Low Energy Band Structure and Symmetries of UTe_2 from Angle-Resolved Photoemission Spectroscopy

Lin Miao,[1,‡] Shouzheng Liu,[2,‡] Yishuai Xu,[2] Erica C. Kotta,[2] Chang-Jong Kang,[3] Sheng Ran,[4,5]
Johnpierre Paglione,[5] Gabriel Kotliar,[3] Nicholas P. Butch,[4,5] Jonathan D. Denlinger,[6,*] and L. Andrew Wray[2,†]
[1]*School of Physics, Southeast University, Nanjing 211189, China*
[2]*Department of Physics, New York University, New York, New York 10003, USA*
[3]*Department of Physics and Astronomy, Rutgers University, Piscataway, New Jersey 08854-8019, USA*
[4]*NIST Center for Neutron Research, National Institute of Standards and Technology,*
100 Bureau Drive, Gaithersburg, Maryland 20899, USA
[5]*Quantum Materials Center, Department of Physics, University of Maryland, College Park, Maryland 20742, USA*
[6]*Advanced Light Source, Lawrence Berkeley National Laboratory, Berkeley, California 94720, USA*

(Received 21 November 2019; accepted 23 January 2020; published 19 February 2020)

The compound UTe_2 has recently been shown to realize spin triplet superconductivity from a nonmagnetic normal state. This has sparked intense research activity, including theoretical analyses that suggest the superconducting order parameter to be topologically nontrivial. However, the underlying electronic band structure is a critical factor for these analyses, and remains poorly understood. Here, we present high resolution angle-resolved photoemission measurements covering multiple planes in the 3D Brillouin zone of UTe_2, revealing distinct Fermi-level features from two orthogonal quasi-one-dimensional light electron bands and one heavy band. The electronic symmetries are evaluated in comparison with numerical simulations, and the resulting picture is discussed as a platform for unconventional many-body order.

DOI: 10.1103/PhysRevLett.124.076401

Recent years have seen a rapid growth in research on tripletlike superconductivity, driven in part by proposed links to Majorana fermion-based quantum information storage [1]. The superconducting state of the heavy fermion compound uranium ditelluride (UTe_2) has recently been proposed as a promising and potentially unique example of such an order parameter emerging from a nonmagnetic normal state [2,3]. However, first principles calculations have predicted a very wide range of underlying band structures [3–7], due in part to the modeling complexity associated with f-electron strong correlations and Kondo lattice physics. Recent soft x-ray angle-resolved photoemission (ARPES) measurements have provided a first look at the electronic structure, but are limited in energy resolution and by strong incoherent scattering at the Fermi level, and have not established a straightforward agreement with numerical simulations [4]. In this Letter, we present high resolution ARPES measurements of the electronic band structure of UTe_2, covering many significant planes in the 3D Brillouin zone. Highly dispersive Fermi level features are shown to correspond closely with first-principles-based simulations combining density functional theory and dynamical mean field theory ($\mathrm{DFT}+\mathrm{DMFT}$). These rectangular Fermi pockets originate from two orthogonal one-dimensional (1D) bands, only one of which has strong uranium character. Nondispersive “heavy” band features associated with the $5f$ orbital of uranium are also discovered, with strong implications for many-body ordering instabilities.

Triplet-based superconductivity is strongly implicated in related uranium compounds such as UGe_2, UReGe, and UCoGe [8–10], where the transition to superconductivity occurs within a ferromagnetic normal state. While UTe_2 does not host long-range magnetic order, the attribution of a nonsinglet order parameter comes from similar factors. For example, the strongly anisotropic upper critical field (H_{c2}) of the UTe_2 superconducting phase is as high as 35 T, which exceeds the Pauli limit for a singlet superconducting pair [11,12], and the Knight shift is anomalously constant through the superconducting transition [2]. The phase diagram under high magnetic fields depicts a regime in which superconductivity can be field stabilized [11,13–15]. The evidence of thermal transport, heat capacity, and magnetic penetration depth measurements suggest pointlike nodal structure that likewise corroborates a triplet superconducting picture [16]. Unconventional Cooper pairing is further suggested by surface probes [17,18] and by measurements showing very strong magnetic fluctuations that coexist with superconductivity [19], and appear to play a role in enhancing the superconducting critical temperature [20].

In this study, ARPES measurements were performed at the MERLIN ARPES endstation beamline 4.0.3 at the Advanced Light Source, and using a helium lamp light source at NYU. The temperature was maintained at $T = 20$ K, and the base pressure was similar to 5×10^{-11} Torr. Samples were prepared in a nitrogen glove box and transferred rapidly to ultrahigh vacuum (UHV) for *in situ* cleavage. After the ARPES experiment, the cleaved sample surface was characterized by x-ray Laue diffraction and the microscope, confirming the (001) cleavage surface (see Supplemental Material [21], Fig. S1). The strongly correlated electronic structure of UTe_2 is modeled using first principles-based dynamical mean field theory (DFT+DMFT) [28–31]. The vertex corrected one-crossing approximation [23] was chosen as the impurity solver, in which the full atomic interaction matrix was taken into account [31]. The Coulomb interaction $U = 6.0$ eV, the Hund's coupling $J = 0.57$ eV, and a nominal double counting scheme were used for the DFT + DMFT calculations. A simplified DFT band calculation was performed for comparison, replacing uranium with thorium within the UTe_2 crystal structure. This removes $5f$ orbitals from the picture near the Fermi level, as thorium strongly favors a vacant quadrivalent thorium $5f^0$ state. Additional discussion of this scenario is provided in the Supplemental Material [21] (see Figs. S2–S4). The DFT calculations in both methods were performed using the full-potential

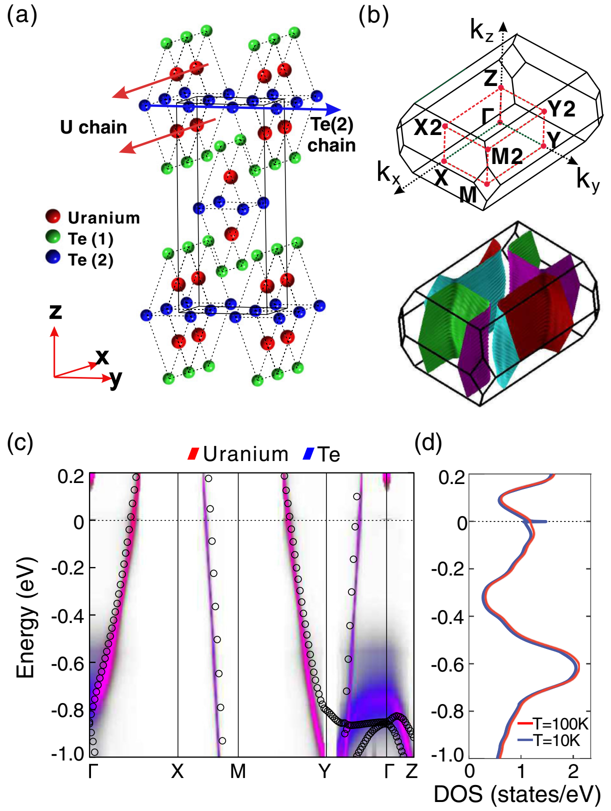

FIG. 1. Quasi-1D sublattices of UTe_2. (a) The crystal structure of orthorhombic UTe_2. The red arrow labels the uranium chain along the *a* axis. The blue arrow labels the Te(2) chain along the *b* axis. (b) The first Brillouin zone of UTe_2 and the DFT-calculated Fermi surface for Th-substituted $ThTe_2$, showing the two light bands. (c) The non-f-orbital DFT band structure (empty circles) is compared with the atomic sites-resolved DMFT + DFT band structure (ribbons) of UTe_2 along k-space paths traced with dashed lines in panel (b). Red and blue shading represent the partial density of states from uranium and tellurium orbitals, respectively. The DFT bands are shifted upwards by 200 meV, for better correspondence with the experimental band structure. (d) The DMFT calculated density of states (DOS) at temperatures of $T = 10$ and 100 K, below and above the onset of Kondo coherence.

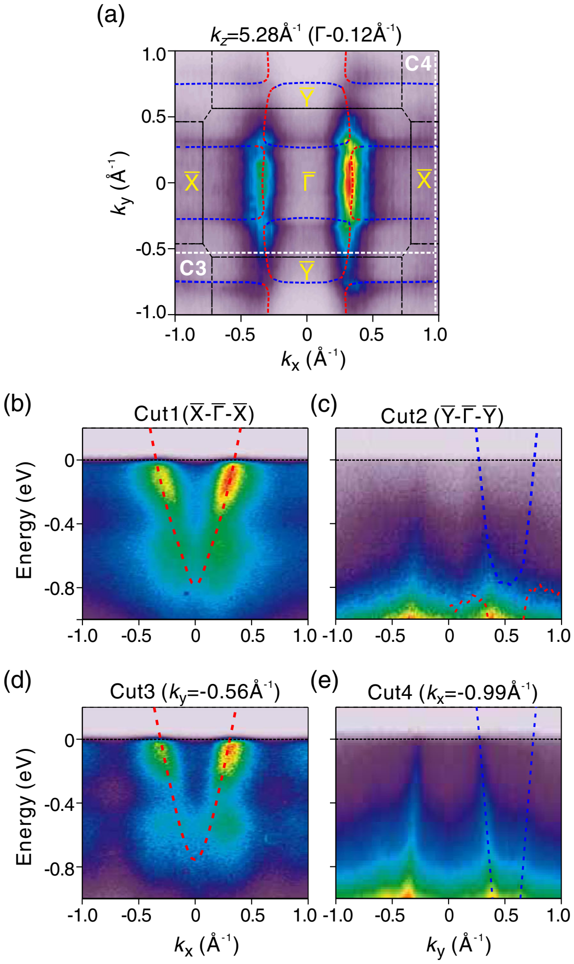

FIG. 2. A quasi-1D by quasi-1D light-band Fermi surface. (a) The ARPES Fermi surface of UTe_2 at the (001) crystal face. All panels are overlaid with the DFT band structure, with the quasi-1D light uranium band drawn in red, and blue lines showing the orthogonally dispersing Te(2) band. (b)–(c) ARPES measurements through 2D Brillouin zone center along the (b) k_x and (c) k_y directions. (d)–(e) Additional measurements that are offset from the Brillouin zone center. The trajectories for these cuts are labeled C3 and C4, respectively, on panel (a). Spectra in panels (a),(b),(d) were measured on the uranium $O_{4,5}$-edge resonance ($h\nu = 98$ eV) to enhance visibility for the U band. Panels (c),(e) were measured off resonance ($h\nu = 92$ eV), and do not include a DFT overlay on the left-hand side for visual clarity.

linearized augmented plane-wave (FLAPW) band method, as implemented in the WIEN2K package [32].

The UTe_2 lattice is orthorhombic, and belongs to the 71-*Immm* space group [33]. As shown in Fig. 1(a), the lattice hosts two significant chainlike structures along orthogonal axes. Uranium atoms appear as dimers that are closely separated along the z axis, and are organized in chains parallel to the x axis, with a trigonal prism of two chemically inequivalent near-neighbor Te sites, labeled Te(1) and Te(2). The plane of Te(2) atoms also form linear chains along the y axis with small nearly uniform 3.1 Å separation, suggesting large hopping mobility along this axis, particularly when compared to the far-larger next-neighbor Te-Te separation of 4.2 Å that occurs along the x axis.

As a first step to understand the electronic structure, we review the simplified DFT simulation in which uranium is replaced with thorium in the crystal to obtain the non-f-electron bands. The resulting Fermi surface consists of four rectangular Fermi pockets, formed by two hybridized bands that have strong 1D character along the k_x and k_y axes [Fig. 1(b)]. The simplified DFT calculation is overlaid on the full DFT + DMFT spectral function in Fig. 1(c), revealing an extremely close visual correspondence. Scrutinizing dispersions near the Fermi level, one can see that the band dispersing along k_x (Γ-X) has primarily uranium character (red shading), while the band dispersing along k_y (Γ-Y) is associated with Te orbitals (blue-purple shading), in keeping with expectations from the crystal structure analysis. A more detailed orbital decomposition is presented in the Supplemental Material [21], Fig. S3, showing that U $6d_{z^2}$ character dominates the electronlike 1D dispersion along k_x and a strong bonding-antibonding splitting of the Te(2) $5p_z$ orbitals is the origin of the holelike 1D Fermi surface sheets. The $5f$ bands are removed from the Fermi level by the large Hubbard U value, a phenomenon also noted as possible in earlier numerical simulations [6,7]. However, examining the density of states reveals a small peak at the Fermi level representing the emergent band structure from Kondo coherence. Though this band is highly significant in defining the low temperature physics of the material, it is not describable by DFT [34], and is essentially invisible within the momentum-resolved electron annihilation spectral function probed by ARPES (see close-up in Fig. S9 [21]).

Overlaying the DFT result on an experimental k_x-k_y plane Fermi surface seen by ARPES at the uranium O-edge resonance ($h\nu = 98$ eV) reveals a very similar checkered structure [Fig. 2(a)]. In this and other comparisons, the non-f-orbital DFT bands are shifted upwards by 200 meV to enhance correspondence with the experimental data. Dispersion measurements performed on resonance show a light band dispersing along k_x with a Fermi velocity that is roughly 50% of the DFT calculation [Figs. 2(b), 2(d)], and

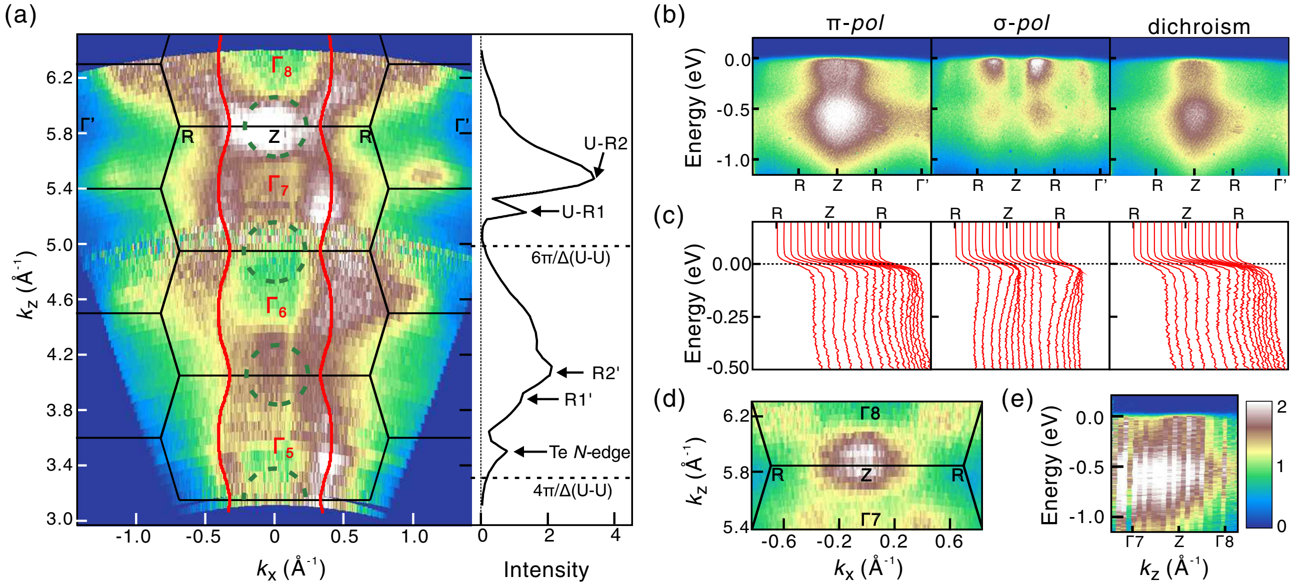

FIG. 3. 3D dispersion and a heavy Z-point electron pocket. (a) The k_x-k_z Fermi surface of UTe_2, measured by tuning incident energy from $h\nu = 30$ to 150 eV (π polarization). The approximate contour of an electron pocket at the Z point is traced in green, and a red curve shows the non-f-orbital DFT-calculated uranium band. The k_x-integrated intensity at the Fermi level is plotted at right, and has been divided out from the image at left for visual clarity. Resonance energies annotated on the intensity curve include the R1 and R2 resonances of the uranium $O_{4,5}$ edge, the 40 eV tellurium N edge, and incoherent background from higher harmonic light intersecting uranium $O_{4,5}$-edge ($R1'$, $R2'$). (b) Polarization-resolved measurements of the Z point ($k_z \sim 5.9$ Å^{-1}, $h\nu = 125$ eV) showing (left) π polarization, (middle) σ polarization, and (right) the dichroic difference [A(π)-A(σ)]. (c) Raw data energy dispersion curves (EDC) for panel (b). (d) A dichroically subtracted Z-point Fermi surface map [A(π)-A(σ)]. (e) The Z-point feature seen in E-k_z dispersion from the panel (a) dataset.

a broad nondispersive feature roughly at 0.7 eV binding energy that has also been noted in an earlier study [4]. The band that disperses along the k_y axis has a negative slope, and closely matches the calculation with a remarkably large band velocity of $v_F \sim 10$ eV Å [Figs. 2(c), 2(e)], that results from the very large 8 eV bonding-antibonding splitting of the Te(2) linear chain p_z orbitals (see Supplemental Material [21], Fig. S4). The quasi-1D nature of these bands at the Fermi level is consistently observed at a range of k_z coordinates in momentum space (see Supplemental Material [21], Fig. S5).

To better understand the three-dimensional electronic structure, k_z axis momentum dependence of the Fermi surface is mapped in Fig. 3(a) over the 5th to 8th Brillouin zones (Γ_5–Γ_8). Overlaying the light uranium band from the non-f-orbital DFT calculation (red curve) reveals a clear periodic correspondence, and yields a very standard inner potential value of $V_0 = 13$ eV for the ARPES k_z calibration. Disregarding core level resonances [labeled on Fig. 3(a), right], the ARPES intensity shows minima and maxima that are approximately periodic with the U-U dimer separation of $\Delta(\text{U-U}) = 3.79$ Å (see dashed lines). Intensity is suppressed at $k_z = n2\pi/\Delta(\text{U-U})$ (for integer n) as expected for a wave function that is largely antisymmetric for reflections of the z axis across the Te(2) plane (see matrix element discussion in Supplemental Material [21], Note 3).

Much of the k_z Fermi surface image in Fig. 3(a) is dominated by a strong and inhomogeneous background from incoherent processes, as is common for incident energy maps in the extreme ultraviolet. Sharp band features are most visible in the 5th and 7th Brillouin zones. Focusing on these regions reveals that the Z point carries enhanced spectral weight (near $k_z \sim 4.1$ and 5.9 Å^{-1}), suggestive of an electronic state that is not visible in the predicted spectral function. This feature has strong polarization dependence, and is almost invisible in a σ-polarization ARPES measurement [Fig. 3(b), center]. Taking the dichroic difference in [Fig. 3(b), right] reveals that it resembles a shallow nondispersive (heavy) state. Examining the k_z axis suggests that the feature may be roughly isotropic in the k_x-k_z plane [see Figs. 3(d), 3(e)], but the large energy width and highly nondispersive nature make it difficult to make a fine determination.

Though the light bands traced in Figs. 2–3 have clean attributions, the more nondispersive features seen at the Z-point Fermi level and at $E = -0.7$ eV do not correspond with prominent features in the calculations. Though DFT + DMFT predicts a DOS maximum with predominant Te character predicted at a similar energy, it does not overlap with these states in momentum space. To better understand this, we examine the difference between measurements performed on- and off-resonance at the uranium O edge [Figs. 4(a)–4(b)]. The O-edge ARPES spectrum clearly enhances final states associated with the light $6d$ uranium band and at ~0.7 eV binding energy, however the heavy Z-point band is not visible as the z-axis momentum is far from the Z point. The $E = -0.7$ eV feature is specifically enhanced at low in-plane momentum ($k_x < 0.5$ Å^{-1}) and has a clear substructure, with two features identifiable in the momentum-integrated intensity, separated by 0.2 eV [Fig. 4(b), red markers]. An O-edge resonant feature with roughly the same k_x resolved intensity profile is visible in ARPES on URu_2Si_2 [35], and $5f^2$ atomic multiplet excitations at ~0.7 eV are the most prominent high energy inelastic features in O-edge resonant inelastic x-ray scattering (RIXS) from $5f^2$ uranium at this photon energy [36]. Examining the DFT + DMFT simulation [Fig. 4(c)], we find that two $5f^2$ atomic multiplet configurations with $^3\text{H}_5$ and $^3\text{F}_2$ symmetry are centered on ~0.7 eV binding energy and separated by 0.2 eV, providing a likely explanation for the feature. If this attribution is correct,

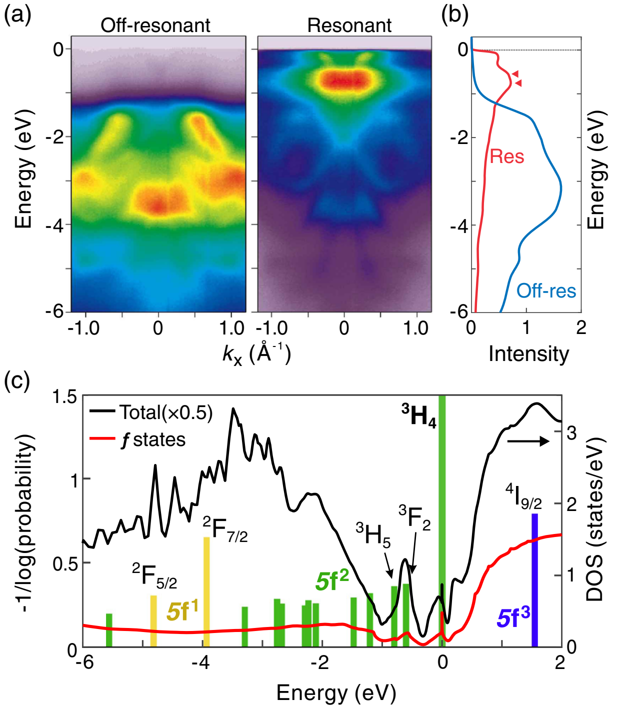

FIG. 4. Comparison between resonant ARPES and off-resonant ARPES. (a) (left) An off-resonance ARPES spectrum with $h\nu = 92$ eV is compared with (right) an on-resonance measurement at $h\nu = 98$ eV (uranium $O_{4,5}$ edge). (c) Momentum-integrated intensity is shown from data in panel (a). These measurements used a different polarization condition than Figs. 2(b)–2(c) (linear horizontal vs circular). Red markers identify dual peaks within the ~0.7 eV binding energy feature. (c) DOS curves from DFT + DMFT are overlaid with bars representing the occupancy of f-orbital atomic multiplet configurations. The $5f^2$ Hund's rule ground state is the dominant configuration ($^3\text{H}_4$, 84% occupancy). The $5f^1$ and $5f^3$ configurations would be associated with lower and upper Hubbard bands, respectively, in the absence of other overlapping bands and interactions.

it strongly supports the picture presented by the numerics of a $^3H_4$-based Kondo lattice.

The heavy Z-point Fermi-level feature has an even more direct significance for correlated physics [17,21,33], and may also provide an important channel for spin-triplet Cooper pairing. Simulations suggest the strongest magnetic interactions between uranium atoms to be ferromagnetic coupling within the uranium dimer, with an energy scale that may rise to tens of millielectron volts [7]. This suggests that triplet-favoring ferromagnetic coupling might be strongest for electrons intersecting on the same dimer. However, Pauli exclusion largely forbids this intersection of spin-aligned electrons if only a single itinerant uranium band is present at the Fermi level, as there will be just one associated Wannier orbital shared by the dimer atoms. The existence of a second uranium band at the Fermi level is thus a prerequisite for strong interactions through this channel, and is fulfilled by the observation of the Z-point pocket. Though we cannot provide a definitive attribution for this Z-point feature from theory, the distribution of intensity is consistent with a shallow electron pocket (see band overlay in the Supplemental Material [21], Fig. S7). The incident energy dependence of this feature is suggestive of a well-defined bonding symmetry within the uranium dimer, and strong suppression under σ (x axis) polarization near the $k_x = 0$ high symmetry plane places further constraints on the observed wave function (see Supplemental Material [21] Note 3).

In summary, we present the electronic band structure study of tripletlike superconductor UTe_2 by high-resolution ARPES. Measurements reveal two light quasi-one-dimensional bands at the Fermi level, that are attributed to uranium and Te(2) chains through an analysis of resonance and dispersion, as well as a comparison with band calculations. A heavy electronic band is observed surrounding the Z point with distinctive reflection symmetry-derived matrix elements, representing an important constituent for heavy Fermion physics. A nondispersive feature at ~0.7 eV binding energy is associated with excitations of a uranium $^3H_5$ and $^3F_2$ atomic multiplet Kondo lattice, through comparison with DFT + DMFT and experimental data on other systems. The significance of this electronic structure for many-body correlations is discussed, and a favorable channel for tripletlike Cooper pairing is proposed.

This research used resources of the Advanced Light Source, which is a DOE Office of Science User Facility under Contract No. DE-AC02-05CH11231. Work at N. Y. U. was supported by the MRSEC Program of the National Science Foundation under Grant No. DMR-1420073. Synthesis and analysis instrumentation at N. Y. U. is supported by NSF under MRI-1531664, and by the Gordon and Betty Moore Foundation's EPiQS Initiative through Grant No. GBMF4838. Research at the University of Maryland was supported by the Department of Energy, Office of Basic Energy Sciences under Award No. DE-SC0019154, and the Gordon and Betty Moore Foundation's EPiQS Initiative through Grant No. GBMF4419. Identification of commercial equipment does not imply recommendation or endorsement by NIST The work at Rutgers was supported by DOE BES Grant No. DE-FG02-99ER45761.

---

[*] jddenlinger@lbl.gov
[†] lawray@nyu.edu
[‡] These authors contributed equally to this work.

[1] C. Nayak, S. H. Simon, A. Stern, M. Freedman, and S. D. Sarma, Rev. Mod. Phys. **80**, 1083 (2008).

[2] S. Ran, C. Eckberg, Q.-P. Ding, Y. Furukawa, T. Metz, S. R. Saha, I.-L. Liu, M. Zic, H. Kim, J. Paglione, and N. P. Butch, Science **365**, 684 (2019).

[3] D. Aoki, A. Nakamura, F. Honda, D. Li, Y. Homma, Y. Shimizu, Y. J. Sato, G. Knebel, J. Brison, A. Pourret, D. Braithwaite, G. Lapertot, Q. Niu, M. Vališa, H. Harima, and J. Flouquet, J. Phys. Soc. Jpn. **88**, 043702 (2019).

[4] S. Fujimori, I. Kawasaki, Y. Takeda, H. Yamagami, A. Nakamura, Y. Homma, and D. Aoki, J. Phys. Soc. Jpn. **88**, 103701 (2019).

[5] A. B. Shick and W. E. Pickett, Phys. Rev. B **100**, 134502 (2019).

[6] J. Ishizuka, S. Sumita, A. Daido, and Y. Yanase, Phys. Rev. Lett. **123**, 217001 (2019).

[7] Y. Xu, Y. Sheng, and Y.-F. Yang, Phys. Rev. Lett. **123**, 217002 (2019).

[8] S. S. Saxena, P. Agarwal, K. Ahilan, F. M. Grosche, R. K. W. Haselwimmer, M. J. Steiner, E. Pugh, I. R. Walker, S. R. Julian, P. Monthoux, G. G. Lonzarich, A. Huxley, I. Sheikin, D. Braithwaite, and J. Flouquet, Nature (London) **406**, 587 (2000).

[9] D. Aoki, A. Huxley, E. Ressouche, D. Braithwaite, J. Flouquet, J.-P. Brison, E. Lhotel, and C. Paulsen, Nature (London) **413**, 613 (2001).

[10] N. T. Huy, A. Gasparini, D. E. de Nijs, Y. Huang, J. C. P. Klaasse, T. Gortenmulder, A. de Visser, A. Hamann, T. Gölach, and H. v. Löneysen, Phys. Rev. Lett. **99**, 067006 (2007).

[11] S. Ran, I.-L. Liu, Y. S. Eo, D. J. Campbell, P. M. Neves, W. T. Fuhrman, S. R. Saha, C. Eckberg, H. Kim, D. Graf, F. Balakirev, J. Singleton, J. Paglione, and N. P. Butch, https://doi.org/10.1038/s41567-019-0670-x.

[12] A. Miyake, Y. Shimizu, Y. J. Sato, D. Li, A. Nakamura, Y. Homma, F. Honda, J. Flouquet, M Tokunaga, and D. Aoki, J. Phys. Soc. Jpn. **88**, 063706 (2019).

[13] D. Braithwaite, M. Valiska, G. Knebel, G. Lapertot, J.-P. Brison, A. Pourret, M. E. Zhitomirsky, J. Flouquet, F. Honda, and D. Aoki, Commun. Phys. **2**, 147 (2019).

[14] W. Knafo, M. Vališa, D. Braithwaite, G. Lapertot, G. Knebel, A. Pourret, J. Brison, J. Flouquet, and D. Aoki, J. Phys. Soc. Jpn. **88**, 063705 (2019).

[15] G. Knebel, W. Knafo, A. Pourret, Q. Niu, M. Vališa, D. Braithwaite, G. Lapertot, M. Nardone, A. Zitouni, S. Mishra, I. Sheikin, G. Seyfarth, J. Brison, D. Aoki, and J. Flouquet, J. Phys. Soc. Jpn. **88**, 063707 (2019).

[16] T. Metz, S. Bae, S. Ran, I.-L. Liu, Y. S. Eo, W. T. Fuhrman, D. F. Agterberg, S. Anlage, N. P. Butch, and J. Paglione, Phys. Rev. B **100**, 220504 (2019).

[17] L. Jiao, Z. Wang, S. Ran, J. O. Rodriguez, M. Sigrist, Z. Wang, N. Butch, and V. Madhavan, arXiv:1908.02846.

[18] S. Bae, H. Kim, S. Ran, Y. S. Eo, I.-L. Liu, W. Fuhrman, J. Paglione, N. P. Butch, and S. Anlage, arXiv:1909.09032.

[19] S. Sundar, S. Gheidi, K. Akintola, A. M. Cote, S. R. Dunsiger, S. Ran, N. P. Butch, S. R. Saha, J. Paglione, and J. E. Sonier, Phys. Rev. B **100**, 140502(R) (2019).

[20] S. Ran, H. Kim, I.-L. Liu, S. Saha, I. Hayes, T. Metz, Y. S. Eo, J. Paglione, and N. P. Butch, arXiv:1909.06932.

[21] See Supplemental Material at http://link.aps.org/supplemental/10.1103/PhysRevLett.124.076401 for additional discussion of sample characterization, numerical modeling, and electronic symmetries, which includes Refs. [22–27].

[22] J. E. Hoffman, K. McElroy, D.-H. Lee, K. M. Lang, H. Eisaki, S. Uchida, and J. C. Davis, Science **297**, 1148 (2002).

[23] Q.-H. Wang and D.-H. Lee, Phys. Rev. B **67**, 020511 (2003).

[24] R. S. Markiewicz, Phys. Rev. B **69**, 214517 (2004).

[25] K. McElroy, G.-H. Gweon, S. Y. Zhou, J. Graf, S. Uchida, H. Eisaki, H. Takagi, T. Sasagawa, D.-H. Lee, and A. Lanzara, Phys. Rev. Lett. **96**, 067005 (2006).

[26] A. Damascelli, Z. Hussain, and Z.-X. Shen, Rev. Mod. Phys. **75**, 473 (2003).

[27] M. Yi *et al.*, Proc. Natl. Acad. Sci. U.S.A. **108**, 6878 (2011).

[28] A. Georges, G. Kotliar, W. Krauth, and M. J. Rozenberg, Rev. Mod. Phys. **68**, 13 (1996).

[29] G. Kotliar, S. Y. Savrasov, K. Haule, V. S. Oudovenko, O. Parcollet, and C. A. Marianetti, Rev. Mod. Phys. **78**, 865 (2006).

[30] K. Haule, C.-H. Yee, and K. Kim, Phys. Rev. B **81**, 195107 (2010).

[31] R. D. Cowan, *The Theory of Atomic Structure and Spectra* (University of California Press, Berkeley, 1981).

[32] P. Blaha, K. Schwarz, G. K. H. Madsen, D. Kvasnicka, and J. Luitz, *WIEN2k* (Karlheinz Schwarz, Techn. Universitat Wien, Austria, 2001).

[33] V. Hutanu, H. Deng, S. Ran, W. T. Fuhrman, H. Thoma, and N. P. Butch, arXiv:1905.04377.

[34] P. Coleman, Heavy fermions and the Kondo lattice: A 21st century perspective, in *Many-Body Physics: From Kondo to Hubbard*, edited by E. Pavarini, E. Koch, and P. Coleman (Forschungszentrum, Jülich, 2015), pp. 1.1–1.34.

[35] J.-Q. Meng, P. M. Oppeneer, J. A. Mydosh, P. S. Riseborough, K. Gofryk, J. J. Joyce, E. D. Bauer, Y. Li, and T. Durakiewicz, Phys. Rev. Lett. **111**, 127002 (2013).

[36] L. A. Wray, J. Denlinger, S.-W. Huang, H. He, N. P. Butch, M. B. Maple, Z. Hussain, and Y.-D. Chuang, Phys. Rev. Lett. **114**, 236401 (2015).

Supplemental Material for

Low energy band structure and symmetries of UTe_2 from angle resolved photoemission spectroscopy

Lin Miao[1, *], Shouzheng Liu[2,*], Yishuai Xu[2], Erica Kotta[2], Chang-Jong Kang[3], Sheng Ran[4,5], Johnpierre Paglione[5], Gabriel Kotliar[3], Nicholas P. Butch[4,5], Jonathan D. Denlinger[6, †], and L. Andrew Wray[2, ‡]

1. School of Physics, Southeast University, Nanjing 211189, China.
2. Department of Physics, New York University, New York, New York 10003, USA
3. Department of Physics and Astronomy, Rutgers University, Piscataway, NJ, 08854-8019, USA
4. NIST Center for Neutron Research, National Institute of Standards and Technology, 100 Bureau Drive, Gaithersburg, MD 20899, USA
5. Quantum Materials Center, Department of Physics, University of Maryland, College Park, MD 20742, USA
6. Advanced Light Source, Lawrence Berkeley National Laboratory, Berkeley, CA 94720, USA

[*] These authors contributed equally to this work

[†] Email: jddenlinger@lbl.gov

[‡] Email: lawray@nyu.edu

Note 1: Evaluation of Fermi nesting by joint density of states (JDOS)

The rectangular Fermi surface imaged in main text Fig. 2(a) is suggestive of strong Fermi surface nesting, raising the question of why the material does not have density wave order. To evaluate this, we have performed joint density of states (JDOS) convolutions [1-4], which correspond roughly with the quasiparticle interference images obtained by scanning tunneling microscopy, and provide a means to identify density wave instabilities. The JDOS amplitude is defined as $N(q) = \Sigma_k A(E_f,k)*A(E_f,k+q)$ where the $A(E_f,k)$ is the Fermi surface density of states. Indeed, using the main text Fig. 2(a) Fermi surface as the template for $A(E_f,k)$ results in a JDOS convolution that shows an extremely strong column-like peak at the k_x Brillouin zone boundary (Fig. S6(a-b)), suggestive of near-neighbor antiferromagnetic correlations along the uranium chain. No analogous feature is visible near the k_y Brillouin zone boundary, as the large velocity of the Te band results in very little density of states at the Fermi level.

However, the appearance of strong nesting is misleading, both because it neglects the significant 3D dispersion identified in the main text Fig. 3(a), and because focusing on the main text Fig. 2(a) Fermi surface excludes the heavy Z-point band. Factoring in the 3D dispersion via a parabolic fit of the two light bands ([Fig. S7) yields a corrected JDOS convolution with only a very weak feature at the Brillouin zone boundary (see Fig. S6(c)). Adding in the heavy Z-point band contributes strong short-wavelength scattering channels, and causes the nesting-associated local maximum to vanish altogether (see Fig. S6(a), red curve). The tendency towards antiferromagnetism along the uranium chain axis is further suppressed by the fact that diagonally coordinated chains are offset by half a unit cell along the x-axis, causing the interchain coupling to be frustrated in this scenario (see Fig. S6(d) diagram). Nonetheless, nesting of the light uranium band will support spin fluctuations that may facilitate Cooper pairing.

Note 2: Fitting of 3D bands' dispersion

The JDOS evaluation is based on the spectra of 3D fitted band structure as shown in Fig. S8, which has involved two procedures: (i) The fitting of electronic band dispersion near the Fermi level as shown in the Fig. S7 and (ii) To apply a Lorentzian broadening to the fitted band dispersion, as described below.

For the quasi-1D uranium band which is normal to k_x-axis, the intensity distribution is given by:

$$I_U(k_x, k_y, k_z) = A(k_y, k_z) * \frac{w}{w^2 + (k_x - x_c)^2}. \qquad (1)$$

In the equation, $A(k_y,k_z)$ is proportional to $1/|\nabla_k E|$, which reflects the Fermi level density of states, and can be calculated from the fitted equation. Also once are k_y,k_z

given, one can also calculate from the fitted band dispersion where the band locates on the k_x axis, x_c. The broadening parameter w is the FWHM for the Lorentzian distribution, and is set to 0.14Å^{-1}.

The impact of the quasi-1D tellurium band to the JDOS is neglectable. It is treated same as uranium band, except that its intensity broadening is along k_y-axis. The band dispersion equation is roughly estimated as E=2.2eV- 16.2eV(Å)^2k_y^2. The intensity of the tellurium band is nearly invisible in Fig.S8(c-d) due to its weak intensity, as a result of the large Fermi velocity of tellurium band.

As for isotropic heavy Z-point electron pocket, the intensity distribution is given by:

$$I(k_x, k_y, k_z) = A * \frac{w}{w^2+|\vec{k}-\vec{r_z}|^2}, \qquad (2)$$

A is a constant to describe the Z-point pocket intensity. $\vec{r_z}$ is where Z point locates, and w is set to be 0.229Å^{-1}, which is the radius for Z-point electron pocket acquired by fitting.

Note 3: Symmetry attribution of the Z-point Fermi level feature

As the Z-point Fermi level feature (referred to as the "Z-pocket" below) cannot be attributed from existing theory, it is useful to briefly discuss symmetry constraints that can be identified from ARPES. We will show that these matrix elements are suggestive of an intradimer bound state with low orbital angular momentum, such as *a heavy 5f band with significant* $|m_j|=1/2$ *angular momentum character*. The Fermi level Kondo coherence feature predicted by DMFT is spread out over momentum space (see Fig. S9), and does not present a dispersive band-like feature to compare with.

Matrix element effects for the Z-pocket include:

(A) It is seen in the 1st Brillouin zone, but appears to be absent near 2nd Brillouin zone Z-points that fall at the edge of the mapping in Fig. 3(a) of the main text (near k_z~4.6, 5.4, and 6.2 Å^{-1}), even where these points intersect the uranium O-edge resonance at k_z~5.4 Å^{-1}.

(B) It is only clearly visible at z-axis momenta that correspond to odd reflection symmetry within the uranium dimers, appearing at Z-points near n~5 and 7, but not visible at n~4, 6, for k_z~nπ/Δ(U-U) where Δ(U-U) is the uranium dimer separation (see Fig. 3(a) of the main text).

(C) It is visible under π-polarization (roughly ***E*** // [0, 0.5, 0.86]), but highly suppressed with σ-polarization (***E*** // [1, 0, 0]). The reflection symmetry of ***A·p*** polarization matrix element for photoemission is convoluted into the spectral function, and defines selection rules with respect to operators that reflect space along the principle axes (R_x,R_y,R_z) [6]. Note that the scattering plane under which we see Z-point electrons in

Fig. 3(a) of the main text is the y-z-plane, and the dispersive axis of the analyzer is normal to this (k_x-resolving).

The implications of these observations are discussed below, and the central message for each point is highlighted in bold.

Though it is not 100% definitive, point (A) suggests that ARPES is showing a signal from states with orbital angular momentum $|m_l|\leq 1$. Orbitals with large angular momentum ($|m_l|>1$ quantized relative to the z-axis are strongly associated with weak normal-emission ($k_x=k_y=0$) matrix elements, because the free particle final state must have no angular momentum about the k_z axis. The fact that the Z-pocket states are visible at normal emission suggests that angular momentum of the associated orbital is not large when quantized relative to the z-axis. The z-axis polarization component in particular should be relatively insensitive to states with $|m_l|\neq 0$ (i.e. orbitals other than $6d_{z2}$ and $5f_{z3}$). Conversely, states with large orbital angular momentum tend to be much more visible in higher Brillouin zones (e.g. see Fig. S2 of Ref. [7] for examples with in-plane polarization). The fact that we do not observe the Z-pocket in the 2nd Brillouin zone (point **(A)** above) suggests that $|m_l|>1$ state components are not dominant. Note that this is consistent with the dispersive uranium 6*d* band, which is associated predominantly with $6d_{z2}$ symmetry ($m_l=0$; see Fig. S3) and is much less visible in the 2nd Brillouin zone.

Point (B) has implications regarding the intra-uranium-dimer bonding symmetry. The safest conclusion that can be drawn from the k_z resonance is that it suggests that the Z-point pocket has low degeneracy (likely just Kramers degeneracy), and does not consist of a near-degenerate bonding/antibonding state pair that might otherwise be expected from the uranium dimer. It is unusual to discuss R_z symmetry, due to the fact that z-axis reflection symmetry is broken by the crystal surface. It is only the (seemingly) clear resonance effects in Fig. 3(a) of the main text, and the tendency towards reflection-symmetric bonding/anti-bonding states in the dimerized uranium sublattice that prompts us to include this in the discussion.

The odd k_z resonance condition suggests that the Z-pocket may have well-defined R_z reflection symmetry within the U dimers. However the R_z symmetry that one attributes depends on the dominant polarization component underlying photoemission. If the matrix element from the z-axis polarization component is dominant, then the R_z symmetry should be even (odd polarization × odd k_z). However, if photoemission comes predominantly from the y-axis component, then the associated R_z symmetry is odd (even polarization × odd k_z).

We note that the asymmetric sensitivity of different orbitals to polarization means that both m_l components within a $m_j=1/2$ state are expected to give the same k_z resonance behavior, consistent with the experimental observation described in point **(B)**. The $m_j=1/2$ state is a superposition of $m_l=1$ and $m_l=0$ states, where the $|m_l|=1$

states are even under R_z (for a reflection plane intersecting the atom) and the $m_l=0$ state is odd. If rotational symmetry about the z-axis is roughly preserved within the uranium dimer, this reversal will cause the $|m_l|=1$ component of the wavefunction to tend to fall in the opposite R_z sector from the $|m_l|=1$ component (for reflection within the Te(2) mirror plane). However, this reversal is counteracted by polarization, as the $|m_l|=1$ component is picked up by the x- and y- components of polarization (R_z even) and the $|m_l|=0$ component is picked up by the z-component (R_z odd). The clean k_z resonance behavior noted in point **(B)** is therefore not incompatible with a photoemission signal sampling both $|m_l|=1$ and $|m_l|=0$ wavefunction components in a strongly spin-orbit-coupled wavefunction.

The reflection symmetries identified from point (C) are compatible with photoemission from the $m_l=0$ orbtial, and suggest that we may have little sensitivity to other orbitals. In this context, it should be noted that the overall orbital matrix element (including the k_z structure factor and interplay with other atoms) is expected to be very different for different m_l states.

The crystal contains R_x and R_y reflection planes that intersect uranium, meaning that these operators relate directly to uranium orbital symmetry. The π-polarization electric field is off-axis within the y-z plane (see point **(C)** above), and reveals states with even R_x reflection symmetry in the $k_x=0$ plane. This suggests that the Z-pocket state must have at least some even-R_x symmetry (along the Z-Γ axis). The σ-polarization condition reveals states that combine even R_y and odd R_x-symmetry. The Z-pocket is strongly suppressed under σ-polarization, suggesting that mixing into these sectors (possible from spin-orbit coupling) may be weak.

The strong preference for π-polarization is consistent with a wavefunction at Z that is even under R_x, such as that of the $m_l=0$ orbital. A coherent spin-aligned superposition of $|m_l|=1$ could also even under R_x, but cannot be created in the spin-orbit coupled m_j basis (j=5/2 sector). Moreover, the $|m_l|=1$ orbitals are picked up by in-plane polarization (see discussion of point **(A)** above) which is much stronger in the σ-polarization measurement condition, meaning that one would not expect an $|m_l|=1$ based photoemission signal from a spin-orbit-mixed state to be suppressed under σ-polarization.

In summary, the ARPES matrix elements of the Z-pocket feature are consistent with a 5f $|m_j|=1/2$ derived bonding state of the uranium dimers, with a photoemission signal dominated by the $m_l=0$ $5f_{z3}$ orbital. This being said, one should of course bear in mind that this train of logic is speculative, and the orbital character may be highly mixed. Spin-orbit coupling ensures some mixing of reflection symmetry, particularly for *f*-electrons. Additionally, we cannot rule out that the Z-pocket may be an emergent feature associated with the delocalization of Kondo singlets. The composite nature of Kondo singlets means that their observed reflection symmetries need not be derived from their dominant orbital character.

Reference:

[1] J. E. Hoffman, K. McElroy, D.-H. Lee, K. M Lang, H. Eisaki, S. Uchida, and J. C. Davis. Imaging quasiparticle interference in $Bi_2Sr_2CaCu_2O_{8+\delta}$. Science **297**, 1148–1151 (2002).
[2] Q.-H. Wang, and D.-H. Lee, Quasiparticle scattering interference in high-temperature superconductors. Phys. Rev. B **67**, 20511 (2003).
[3] R. S. Markiewicz, Bridging k and q space in the cuprates: comparing angle-resolved photoemission and STM results. Phys. Rev. B **69**, 214517 (2004).
[4] K. McElroy, G.-H. Gweon, S. Y. Zhou, J. Graf, S. Uchida, H. Eisaki, H. Takagi, T. Sasagawa, D.-H. Lee, and A. Lanzara, Elastic scattering susceptibility of the high temperature superconductor $Bi_2Sr_2CaCu_2O_{8+\delta}$: a comparison between real and momentum space photoemission spectroscopies. Phys. Rev. Lett. **96**, 067005 (2006).
[5] Y. Xu, Y. Sheng, and Y.-F. Yang, Phys. Rev. Lett. **123**, 217002 (2019).
[6] A. Damascelli, Z. Hussain, and Z.-X. Shen, Angle-resolved photoemission studies of the cuprate superconductors. Rev. Mod. Phys. **75**, 473 (2003)
[7] M. Yi *et al.*, Symmetry-breaking orbital anisotropy observed for detwinned $Ba(Fe_{1-x}Co_x)_2As_2$ above the spin density wave transition, Proc. Natl. Acad. Sci. USA, **108**, 6878-6883 (2011).

Fig. S1

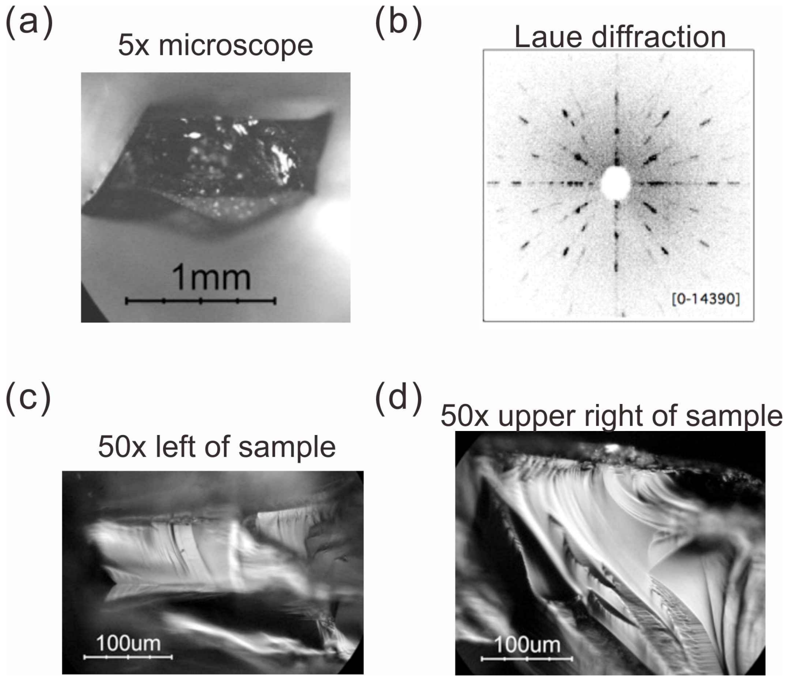

Fig. S1. The characterization of cleaved UTe_2. (a) The cleaved sample surface under 5x microscope. (b) Normal incidence X-ray Laue diffraction from the cleaved UTe_2 sample indicating a (001) cleavage orientation. Most samples cleaved along other orientations, resulting in non-(001) Laue patterns (not shown; such samples were excluded from this study). (c) The zoom-in (x50) image of a shiny and relatively flat area at the left part of UTe_2 sample. (d) A larger shiny flat area at the upper right part of UTe_2 sample, where the ARPES measurements were taken.

Fig. S2

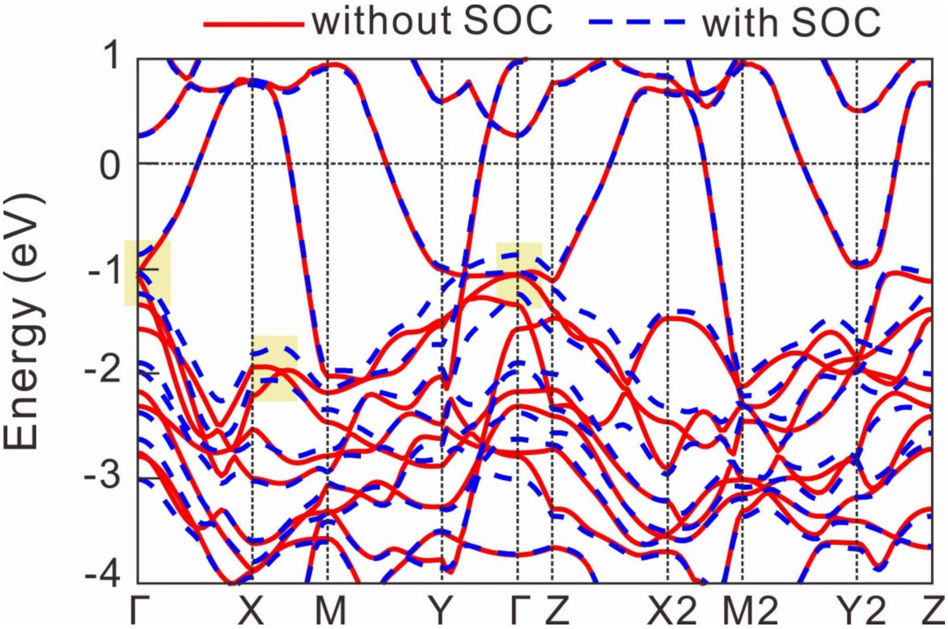

Fig. S2. The comparison of $ThTe_2$ DFT without spin-orbital coupling (red lines) and with (blue dashed lines). The inclusion of SOC in the DFT calculations lifts degeneracies at some points (shaded in the yellow). However, the impact of SOC is minimal near the Fermi level in these calculations.

Fig. S3

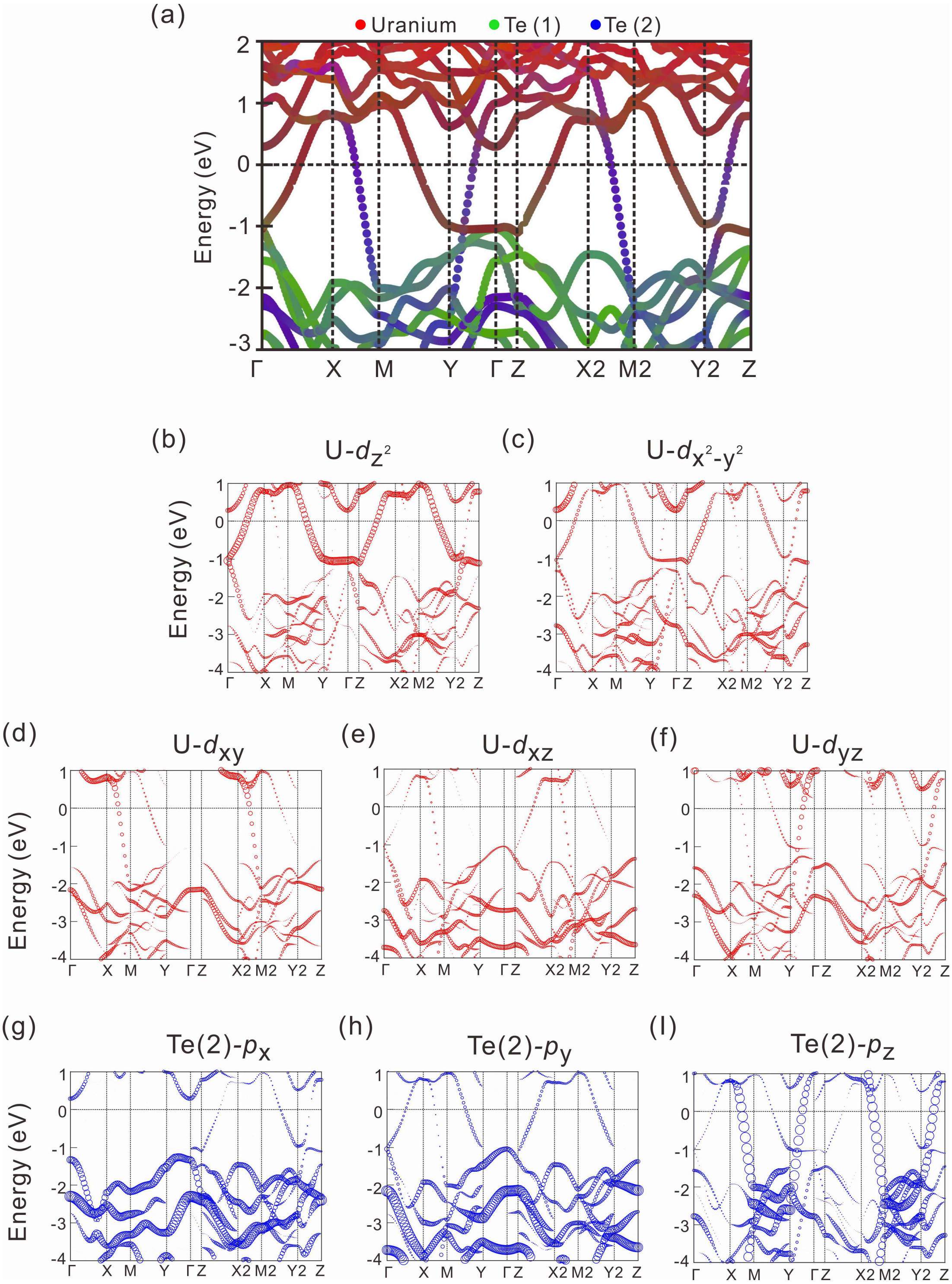

Fig. S3. The orbital-resolved partial density of states from $ThTe_2$ DFT. (a) The atomic sites-resolved DFT-calculated band structure of UTe_2. It is plotted with a rectangle path in the Brillouin zone (main text Fig.1(b)). The RGB color system is used to represent the density of states at the atomic sites, e.g. uranium is noted with red, Te(1) is noted with green, Te(2) is noted with blue. (b-f) The PDOS of different 6*d*-orbital symmetries for uranium sites are shown, revealing large 6d_{z2} character in the Γ-X dispersive band. (g-i) The PDOS within tellurium 5*p* orbitals for the Te(2) sites, revealing the Γ-Y dispersive band to have large 5p_z character.

Fig. S4

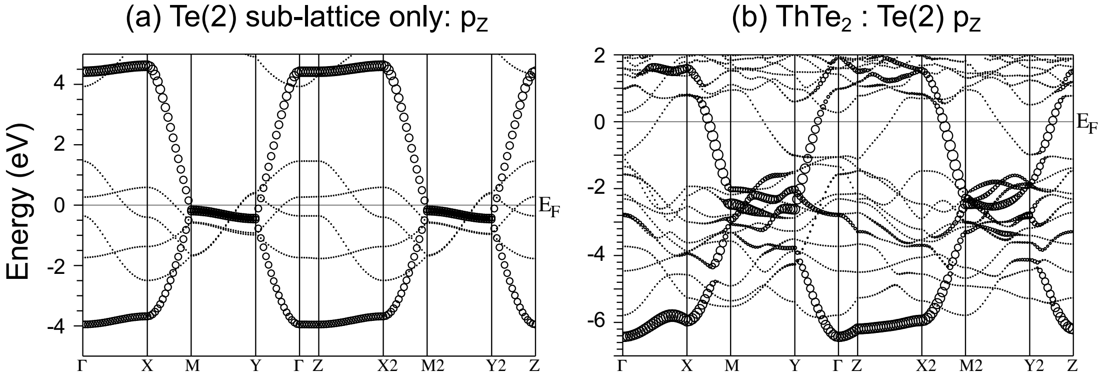

Fig. S4. Te(2) linear chain electronic structure. (a) The band structure of the Te(2) site planar sublattice reveals a large 8 eV bonding-antibonding splitting of the p_z orbitals resulting from the small ≈*b*/2=3.1 Å near-neighbor distance along y-axis linear chains. (b) The large Te(2) bonding-antibonding splitting relative to other Te(2) or Te(1) p-orbital bands enables the existence of the hole-like 1D Fermi surface sheets with large band velocity in ThTe$_2$.

Fig. S5

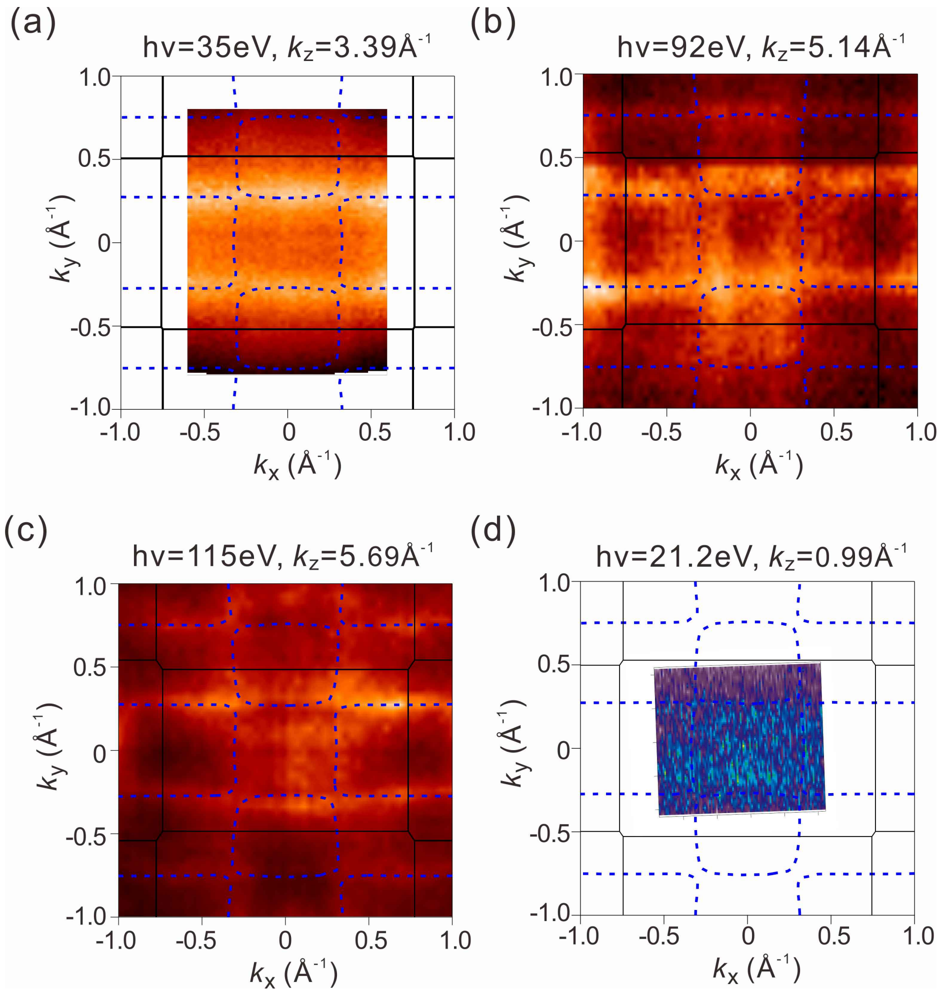

Fig. S5. The Fermi surface of UTe_2 under different incident photon energies. Rapid scans of the Fermi surface were performed with photon energy of (a) hv=35eV, (b) hv=92eV, (c) hv=115eV and (d) hv=21.2eV, and overlaid with the Fermi surface from $ThTe_2$ DFT.

Fig. S6

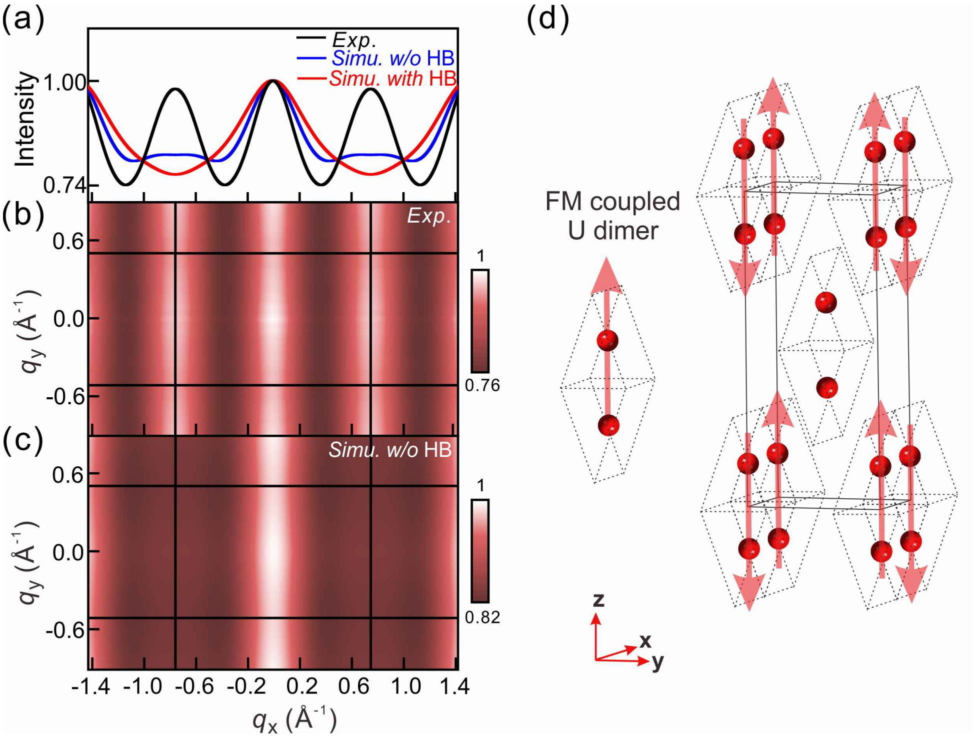

Fig. S6. Weak Fermi surface nesting. (a) Nesting JDOS curves averaged over q_y are obtained from (black) the main text Fig. 2(a) $k_x - k_y$ Fermi surface, (blue) a 3D-fitted band structure neglecting the Z-point heavy electron band (HB), and (red) the fitted band structure incorporating the heavy Z-point band. The octagonal Brillouin zone is simplified to a rectangle, due to the limited range of the main text Fig. 2(a) template. (b-c) Full $q_x - q_y$ plane results of (b) the main text Fig. 2(a) experimental data convolution and (c) the fitted band structure convolution. (d) A diagram shows an antiferromagnetic structure previously considered in previous DMFT numerics [5], in which magnetic coupling to the central uranium dimer chain is geometrically frustrated.

Fig. S7

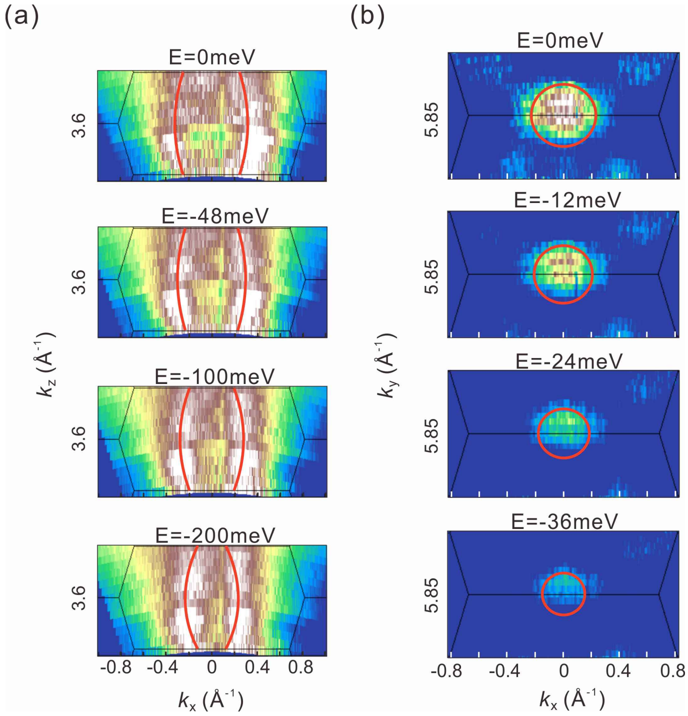

Fig. S7. The fitting of uranium light and heavy band pockets (a) The fitting of uranium light band by using equation $E=0.416eV*(-1+k_x^2/a+ k_y^2/b+ k_z^2/c)$ where $a=0.313$Å^{-1} (from fitting), $b=1.103$ Å^{-1} (from DFT calculation) and $c=0.729$ Å^{-1} (from fitting). (b) The fitting of heavy band at z-point by using equation $E=0.061eV*(-1+k_x^2/0.229\ (Å^{-1})^2+ k_x^2/0.229(Å^{-1})^2+ k_z^2/0.229(Å^{-1})^2)$ with the assumption of an isotropic Fermi pocket.

Fig. S8

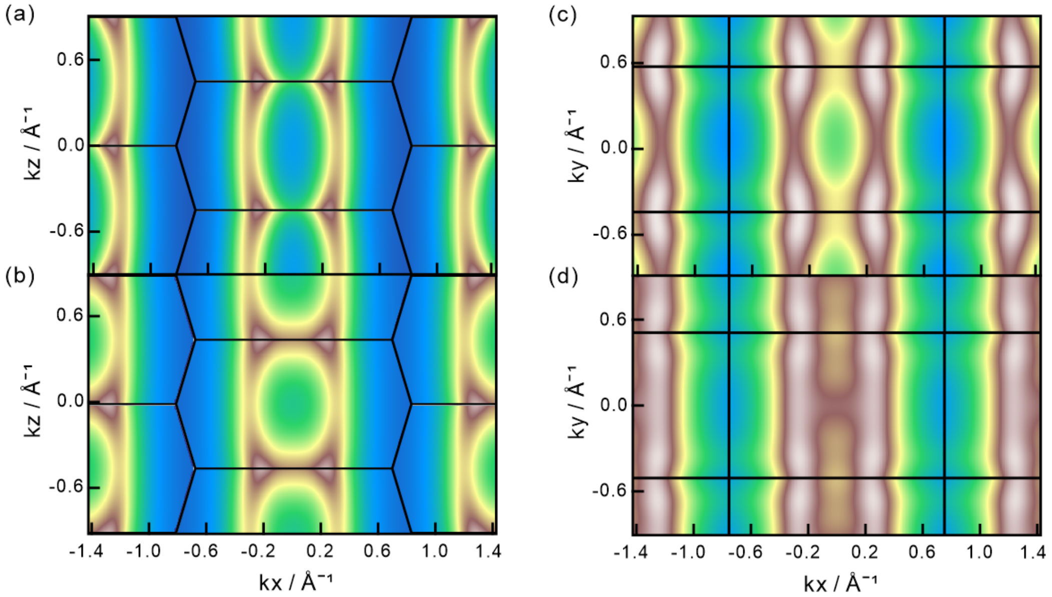

Fig. S8. Simulated Fermi surface from fitted band equations (a-b) Fitted uranium bands in k_x-k_z plane (k_y=0) without (a) and with (b) the heavy Z-point electron pocket. The spectra are with k_y integrated from -0.20Å^{-1} to 0.20Å^{-1}. (c-d) Fitted uranium bands in k_x-k_y plane (k_z=0.225 Å^{-1}) without (c) and with (d) heavy Z-point electron pocket. The spectra are with k_z integrated from 0 to 0.45 Å^{-1}.

Fig. S9

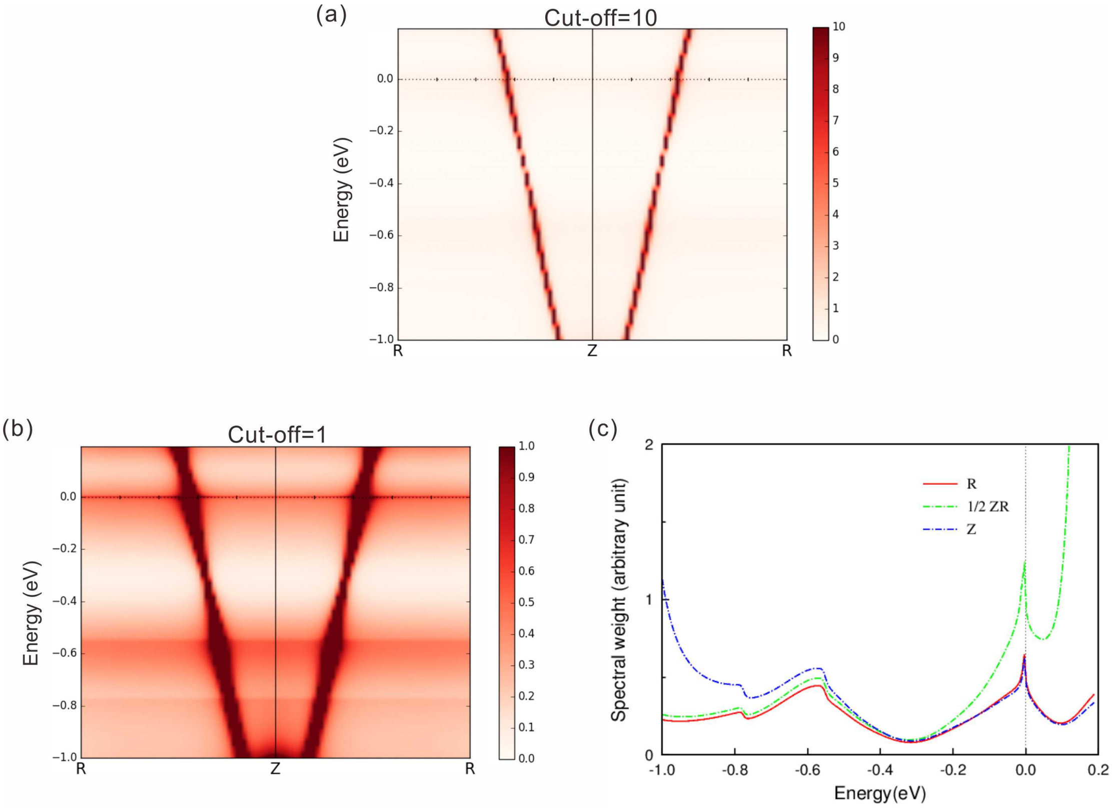

Fig. S9. The momentum-resolved *f*-orbital states at Fermi level. (a-b) The DFT+DMFT calculated low-temperature (T=10K) electronic band structure along the k-space R-Z-R path with (a) large and (b) small color-scale maxima for spectral intensity. The R-point is midway between the 'X' and 'X2' points identified in Fig. 1 of the main text (see k-space diagram in Fig. 2(d) of Ref. [5]). (c) The spectral weight distributions at different momenta extracted from panels (a-b). The spectrum is orbital-integrated, and not constrained by photoemission matrix elements.